Chemical reaction directed oriented attachment: from precursor particles to new substances

Yongfei Liu[1], Xiaoying Qin[1], Yong Yang[1], Zhi Zeng[1], Hongxing Xin[1], Zhengfei Dai[1], Chunjun Song[1], Xiaoguang Zhu[1], Di Li[1], Jian Zhang[1] & Yoshiyuki Kawazoe[2,3]

[1]Key Laboratory of Materials Physics, Institute of Solid State Physics, Chinese Academy of Sciences, Hefei 230031, China.

[2]New Industry Creation Hatchery Center (NICHe), Tohoku University, 6-6-4 Aoba, Aramaki, Aoba-ku, Sendai, Miyagi 980-8579, Japan.

[3]Institute of Thermophysics, Siberian Branch of Russian Academy of Sciences, Novosibirsk 630090, Russia.

As a nonclassical crystal growth mode, oriented attachment (OA) plays an increasingly important role in materials science and nanotechnology, and has shown great significance in the development of crystal growth theory[1]. The OA process usually involves the oriented self-assembly of primary nanoparticles and conversion to single crystals or pseudocrystals by interface fusion[2,3] (Fig. 1a). It is theorized that the OA process is dominant in the early stage of crystal growth[4], driven by the Brownian motion or short-range interactions[2,5]. Such oriented alignments usually can be achieved under hydrothermal/solvothermal conditions[1,6,7] or with the assistance of surfactants[8-11] (Fig. 1b). In conventional OA growth, the constituent and phase structure of the formed crystals are identical to those of the precursor nanocrystals. Here we report a chemical reaction directed OA growth that can create new substances from the precursor nanoparticles (Fig. 1c). Specifically, we show that through such a new OA mechanism, $Y_2(CO_3)_3 \cdot 2H_2O$ nanoparticles can grow into single-crystalline sandwich-structured $NaY(CO_3)_2 \cdot 6H_2O$ and $(NH_4)Y(CO_3)_2 \cdot H_2O$ microsheets by reacting with $NaHCO_3$ and NH_4HCO_3, respectively. The assembled architectures are characterized by layer and spiral growth and other interesting features, such as kinks, terraces, and steps, indicating that during the OA process the nanoparticles behave as atoms or molecules do in the classical mode of crystal growth. Such a chemical reaction directed OA growth can be applied to the synthesis of other alkali-metal rare-earth double carbonates. Our first-principles calculations demonstrate that the intercalation reaction plays a dominant role in the formation of the yttrium double carbonates. Present findings not only enrich the aggregation-based crystal growth theory, but also pave a new way for designing advanced functional materials from the elementary nanoparticles.

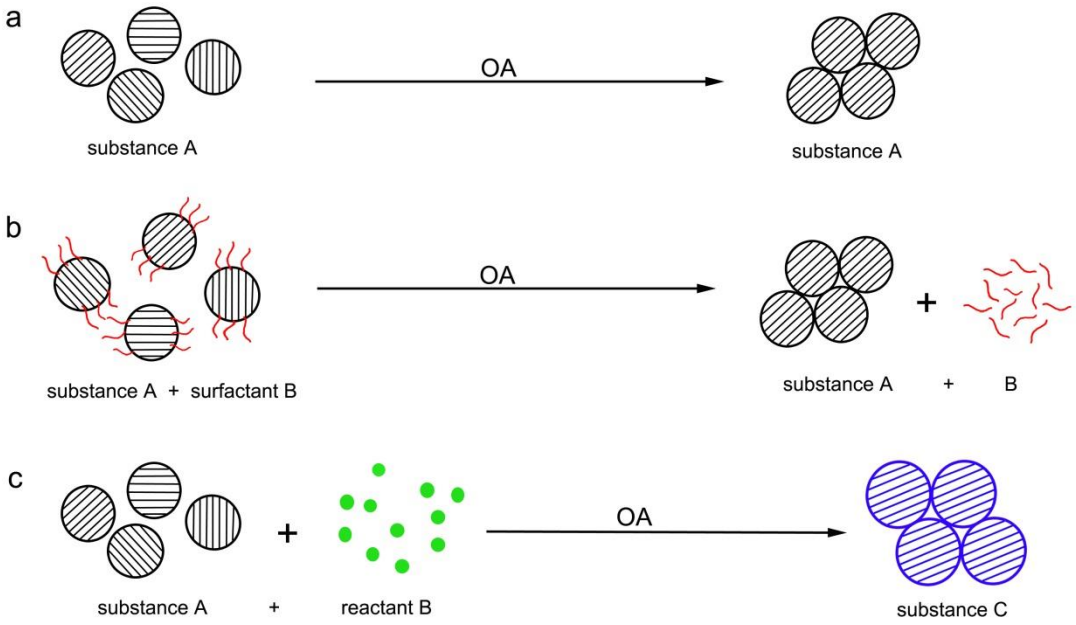

Figure 1 | Schematics of conventional OA processes (a and b) and chemical reaction directed OA process (c). a, The oriented alignments of primary nanoparticles and fusion to form a single crystal. **b,** With the assistance of surfactants (red wavy lines) a single crystal grows via oriented alignments and fusion of primary nanoparticles. **c,** New single-crystalline substance forms accompanying the alignment and reorganization of precursor nanoparticles while reacting with introduced reactants.

OA growth of precursor nanoparticles into new compounds. In a typical synthesis protocol, the precursor $Y_2(CO_3)_3 \cdot 2H_2O$ nanoparticles were fabricated via a conventional precipitation method[12]. To the suspensions, $NaHCO_3$ and NH_4HCO_3 aqueous solutions at the desired concentration were added as reactants under vigorous stirring, respectively. After reaction for 10-120 min, single-crystalline double-carbonates of $NaY(CO_3)_2 \cdot 6H_2O$ and $(NH_4)Y(CO_3)_2 \cdot H_2O$ sheets of micrometer sizes (labeled as Y1 and Y2, respectively) were successfully synthesized. Details of the synthesis procedure can be found in the Methods section.

We performed transmission electron microscopy (TEM), field-emission scanning electron microscopy (FESEM), atomic force microscopy (AFM), powder X-ray diffraction (PXRD), and small angle X-ray scattering (SAXS) analyses on the precursor nanoparticles and the synthesized sheet-like double-carbonates. The TEM image of the precursor (Fig. 2a) shows that it is composed of weakly flocculated nanoparticles with sizes ranging from ~ 10 to 60 nm, in good agreement with SAXS measurements (Fig. 2e). In contrast, the obtained sheets possess rectangular and rhombic shapes in lateral sizes up to ~ 10 μm (Figs. 2b, 2c, Extended Data Fig. 1). The selected-area electron diffraction (SAED) patterns (insets of Figs. 2b, 2c) verify that these micron-sized sheets are single crystals. The PXRD patterns (Fig. 2f) confirm that the precursor nanoparticles and the obtained sheets are $Y_2(CO_3)_3 \cdot 2H_2O$ (orthorhombic, JCPDS card No. 81-1538),

$NaY(CO_3)_2\ 6H_2O$ (anorthic, JCPDS card No. 54-0703), and $(NH_4)Y(CO_3)_2\ H_2O$ [Extended Data Discussions], respectively. This result indicates that both chemical constituents and crystal structures have changed after the growth, leading to the formation of new substances.

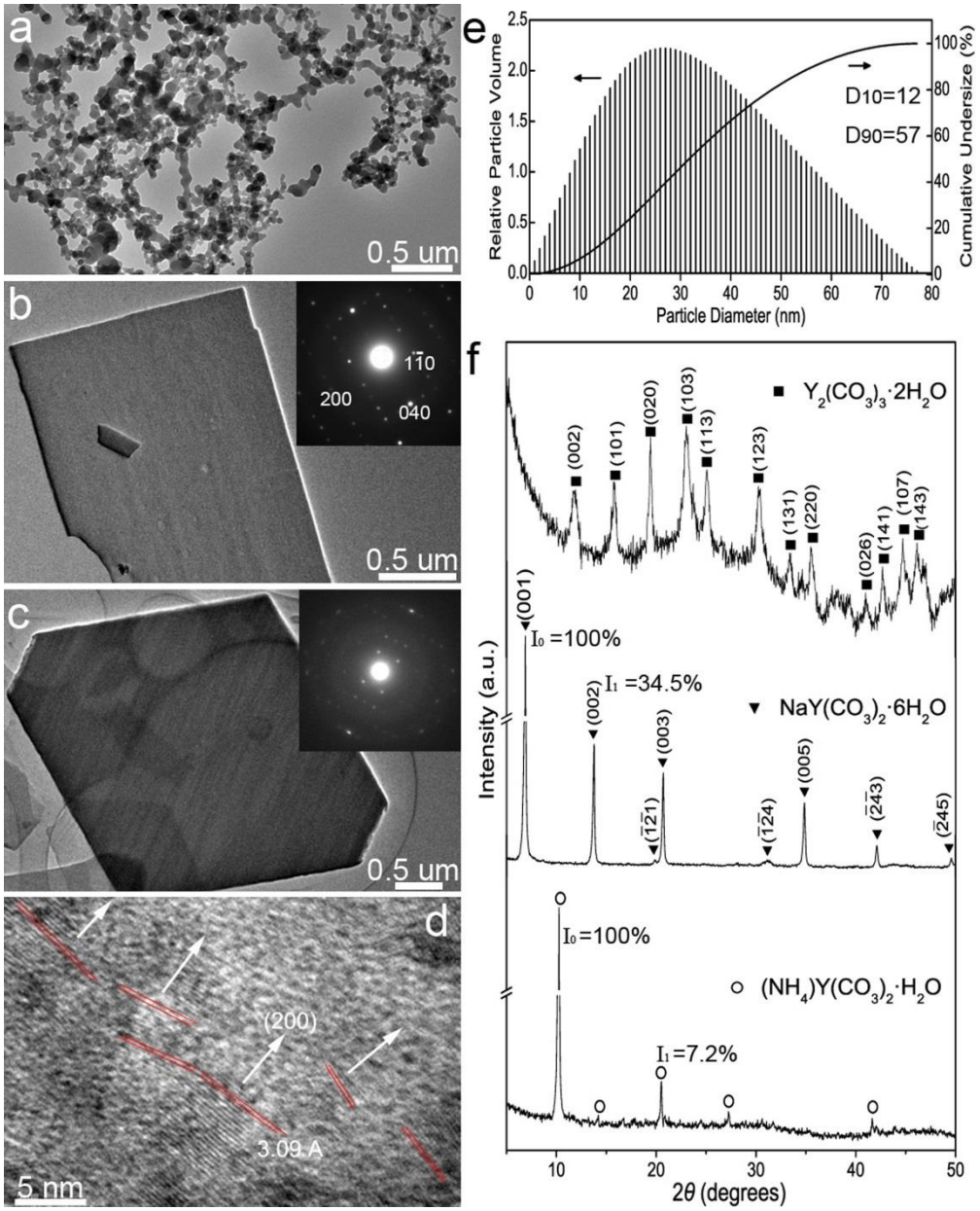

Figure 2 | Characterization of the precursors and products. (a-c) TEM images of precursor nanoparticles and the two obtained sheets (Y1 and Y2). Insets are corresponding SAED patterns. **d,** HRTEM image of Y1 sheet. Imperfect oriented attachments can be identified as indicated by the red lines. **e,** Particle size distribution of the precursor nanoparticles measured by SAXS. **f,** PXRD patterns of the precursor nanoparticles and obtained sheets, corresponding to orthorhombic $Y_2(CO_3)_3\ 2H_2O$, anorthic $NaY(CO_3)_2\ 6H_2O$ and $(NH_4)Y(CO_3)_2\ H_2O$ phases, respectively.

Our high resolution TEM (HRTEM) images show that many regular lattice domains (Fig. 2d and Extended Data Fig. 2) in an average size of ca. 5 nm exist in the grown $NaY(CO_3)_2 \cdot 6H_2O$ single crystal, which is hardly understood by the classical ion-by-ion growth mode. The sizes of these domains are comparable to the primary particles of the precursors (Extended Data Fig. 2b). Such aligned structures and the correspondence between the domains in the grown crystal and the primary particles of precursors strongly indicate an oriented attachment of nanoparticles. Though the clear lattice-fringe image of $(NH_4)Y(CO_3)_2 \cdot H_2O$ sheet cannot be obtained due to the rapid beam damage in TEM observations (Extended Data Fig. 3), the sharp XRD peaks (at 2θ=6.88 ° for $NaY(CO_3)_2 \cdot 6H_2O$ and 10.21 ° for $(NH_4)Y(CO_3)_2 \cdot H_2O$) suggest their high crystallinity and oriented growth[13].

Granular nature of the fracture surfaces for the grown sheets. As revealed by the FESEM inspections, the two sheets show parallel edges, spiral patterns (Figs. 3a, 3d, and Extended Data Fig. 1), and other surface defects such as steps, terraces and kinks (indicated by arrows in Fig. 3d), which are reminiscent of the classical crystal growth that involves the atom-by-atom attachment[14]. Nevertheless, detailed FESEM/AFM observations show that the fracture surfaces of the sheets have granular fracture nature (indicated by red arrow 3 in Fig. 3b, Figs. 3e-f), indicating that they consist of nanoparticle assemblies. The exposed particles are typically around 18-53 nm (Extended Data Fig. 4) in size, and the step is ~ 34 nm in height (inset of Fig. 3f), as revealed by cross-sectional analyses using AFM. One can also find this particle-assembly characteristic from the vertical plane of the fracture (indicated by red arrow 4 in Fig. 3c). Such fractures cannot be obtained from the single crystal grown through atom-by-atom attachments, which usually exhibit cleavage fractures with smooth planes (especially for brittle materials such as salts). In contrast, during the OA process the surfaces of nanoparticles are not atomically flat and the size of the nanoparticles is much larger than atoms/ions. Imperfect alignments of nanoparticles and incomplete interface fusion occur frequently, which inevitably results in the formation of defect-rich regions at the interfaces of the precursor nanoparticles[3]. While the OA grown single crystals fracture, the cracks will propagate along these defect-rich interface regions and the fracture surfaces will show granular feature, and thus exposing characteristics of nanoparticle assemblies. Such features are not observed on the Si substrates (indicated by green arrows 1 and 2 in Fig. 3), even on the unbroken surfaces of the sheets (blue arrow 5 in Fig. 3c), indicating that these granular fractures do not come from the deposition of nanoparticles but are the inherent nature of the sheets. Hence, present observations further verify that the single crystalline sheets originate from the oriented attachment of nanoparticles.

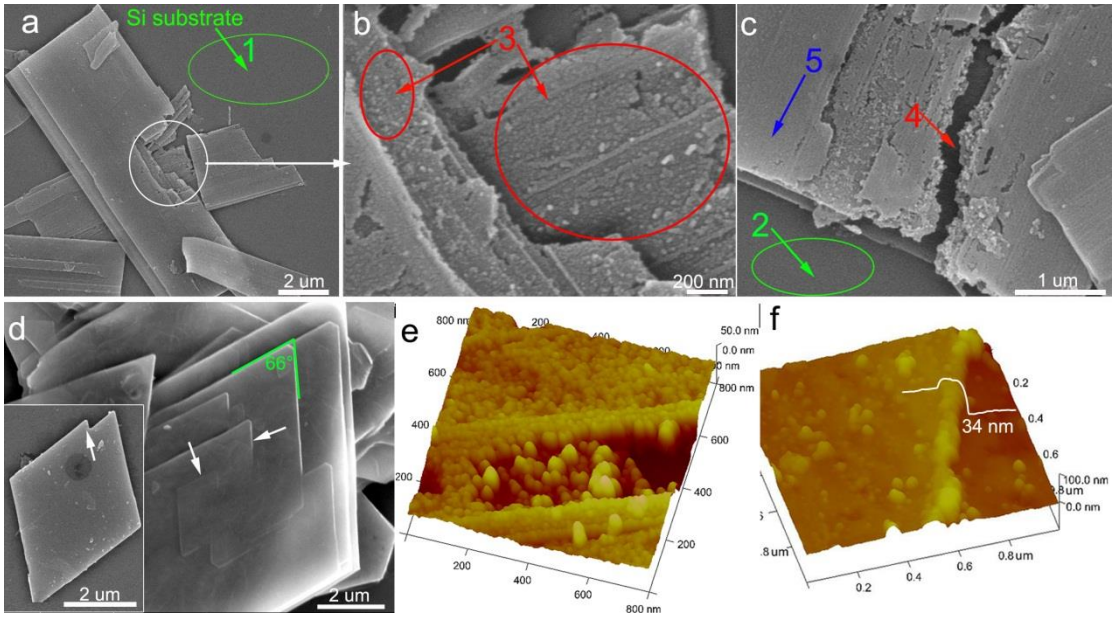

Figure 3 | Surface morphology of $NaY(CO_3)_2\cdot 6H_2O$ and $(NH_4)Y(CO_3)_2\cdot H_2O$. a-c, FESEM images and **e**, 3D AFM surface plot of broken $NaY(CO_3)_2\cdot 6H_2O$ sheets. **d**, FESEM image and **f**, 3D AFM surface plot of $(NH_4)Y(CO_3)_2\cdot H_2O$ sheets. The inset line in **f** shows the cross-sectional analysis of the step site.

The microstructures of the intermediates. We further study the formation of intermediates for $NaY(CO_3)_2\cdot 6H_2O$ sheets taken from the suspension synthesized at 0.2 M of $Y(NO_3)_3$ solution and 1 M $NaHCO_3$ solution after reaction for 1 hr. One can see that on the sheets there are some "unmatured" areas (Extended Data Fig. 5), which show network-like structure consisting of aggregated particles. SAED pattern shows the single crystalline nature of the matured sheet (Extended Data Fig. 5c), while the HRTEM images of the networks indicate that they consist of particles with disordered orientations (Extended Data Fig. 5d). Such features exclude the possibility that this kind of networks come from the partial dissolution of the pristine single crystalline sheets; for if they were, the networks should still show aligned lattice fringes rather than random ones. The network-like structures are the intermediates between the starting particles and the final sheets. The SEM and TEM images for the intermediate products sampled during the formation of $(NH_4)Y(CO_3)_2\cdot H_2O$ sheets (Extended Data Fig. 6) lead to the inference that the sheets are grown through nanoparticle assembly, i.e., OA instead of the classical mode.

Particle assembly in the OA grown sheets revealed by etching-treatment of defect-rich regions. Generally, OA and Ostwald ripening (OR) mechanisms coexist during the crystal growth[4], and the latter can promote the elimination of grain boundaries and surface reconstruction[15,16]. However, as mentioned above, defect-rich regions exist in the OA grown crystals and these regions can be etched preferentially by chemical etching due to their higher energy. In order to uncover these defect-rich regions in the smooth $(NH_4)Y(CO_3)_2\cdot H_2O$ sheets,

hydro/solvothermal treatments were conducted at temperature of 160 ℃ for 24 hrs in ethanol, ionized water and toluene, respectively. The etching reaction was tuned by controlling the addition of NH_3•H_2O, which can regulate the concentration of NH_4^+ and thus ensures that the defect-rich regions can be etched preferentially (see Extended Data Fig. 7 and Fig. 8 for details). Figures 4a-c show the FESEM images of the sheets after being treated in ethanol. It can be clearly seen that the etched sheets are composed of regular particle array patterns in which the particle arrangements are highly ordered and have the same shape as the pristine rhombic sheets. Similarly, the sheets show rhombic patterns to which some scattered nanoparticles cling after being treated in both toluene (Figs. 4d-e) and ionized water (Fig. 4f). The acute angles of the rhombic frameworks are about 65°~68°, matching that of the pristine sheets (66°, as shown in Fig. 3d). Such regular particle patterns cannot be obtained by etching a single crystal grown from the classical mode. Present observations reveal the intrinsic microstructures of pristine sheets, indicating the nanoparticle aggregation-based crystal growth.

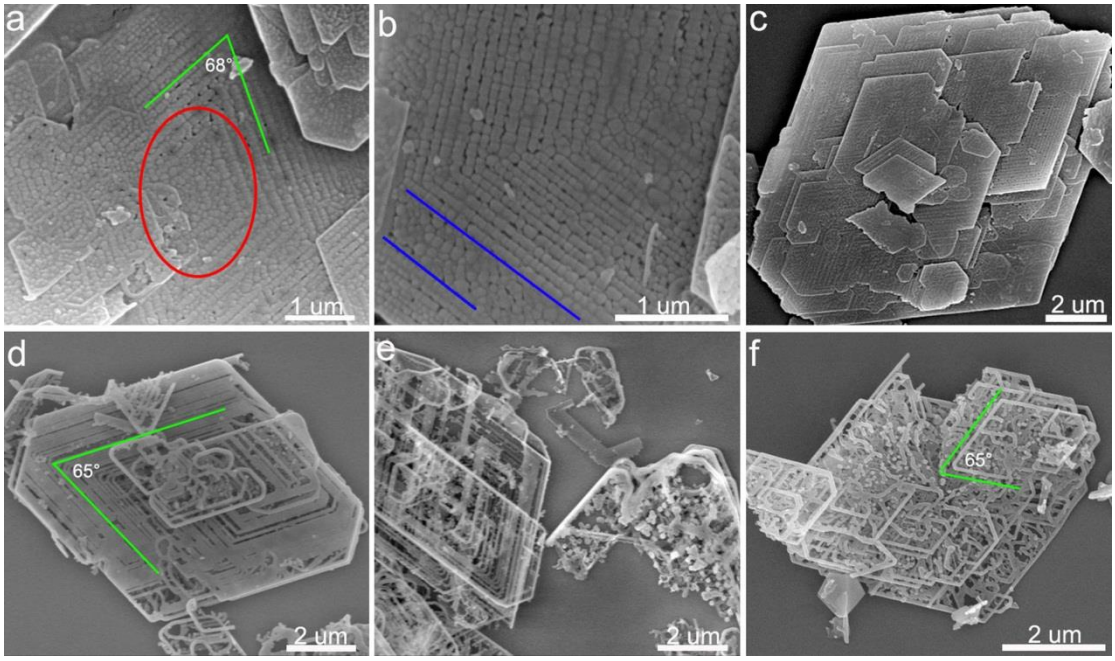

Figure 4 | FESEM images of the $(NH_4)Y(CO_3)_2$ H_2O sheets after post-treatment in: (**a-c**) ethanol, (**d, e**) toluene, and (**f**) ionized water, respectively. Typically, $(NH_4)Y(CO_3)_2$ H_2O suspensions (3 ml) were mixed with 3 ml NH_4OH solution (1.0 M) into 45 ml of solvents (ionized water, absolute ethyl alcohol, and toluene, respectively), and then aged at 160 ℃ for 24 hrs.

The role of the chemical reaction in the OA process. It is obvious that chemical reactions between $Y_2(CO_3)_3$ $2H_2O$ nanoparticles and CO_3^{2-}, Na^+, or NH_4^+ play a decisive role in the formation of single crystalline $NaY(CO_3)_2$ $6H_2O$ (or $(NH_4)Y(CO_3)_2$ H_2O) sheets through the OA

of precursor nanoparticles ($Y_2(CO_3)_3 \cdot 2H_2O$). To examine the effects of the chemical reaction on the OA growth, the introduced reactants of $NaHCO_3$ and NH_4HCO_3 solutions were replaced by NaOH and NH_4OH solutions (with the same concentration), respectively. FESEM observations show that no micron-sized or nano-sized sheets are obtained (Extended Data Fig. 9). This result indicates that the chemical reaction of the introduced reactants with $Y_2(CO_3)_3 \cdot 2H_2O$ to form double-salts are prerequisite to such an OA growth, since no double carbonates are produced through the addition of NaOH or NH_4OH. Moreover, we try to use this strategy to synthesize other alkali-metal rare-earth double carbonates, such as $NaGd(CO_3)_2 \cdot 6H_2O$ and $KNd(CO_3)_2 \cdot xH_2O$. Single crystalline sheets can also be obtained through the reactions of $Gd_2(CO_3)_3 \cdot 2H_2O$ (or $Nd_2(CO_3)_3 \cdot 2H_2O$) nanoparticles with $NaHCO_3$ (or $KHCO_3$), as shown in Extended Data Fig. 10, further evidencing the pivotal role of the reaction to form double-salts in the OA growth.

The mechanism of the chemical reaction directed OA. The most interesting issue is how the chemical reaction can give rise to the OA growth of the yttrium double carbonates ($NaY(CO_3)_2 \cdot 6H_2O$ and $(NH_4)Y(CO_3)_2 \cdot H_2O$). The layer structured $Y_2(CO_3)_3 \cdot 2H_2O$ consists of YO_9 polyhedra[17] and the sandwich structured yttrium double carbonates consists of YO_9 polyhedra layers together with $Na(CO_3) \cdot H_2O$ or $NH_4(CO_3) \cdot H_2O$ layers[18]. Therefore, the reactions are likely to take place through the approach of ion intercalations (CO_3^{2-}, Na^+ or NH_4^+) into the gallery space of $Y_2(CO_3)_3 \cdot 2H_2O$ lattice (Extended Data Fig. 11) due to the insolubility of $Y_2(CO_3)_3 \cdot 2H_2O$ ($K_{sp} = 1.03 \times 10^{-31}$ at 25 ℃)[19], as follows:

$$Y_2(CO_3)_3 + 2Na^+ + CO_3^{2-} + 12H_2O \rightarrow 2NaY(CO_3)_2 \cdot 6H_2O \quad (1),$$

$$Y_2(CO_3)_3 + 2NH_4^+ + 3CO_3^{2-} + 2H_2O \rightarrow 2(NH_4)Y(CO_3)_3 \cdot H_2O \quad (2),$$

The large gallery space in the (100) plane (Extended Data Fig. 11) can serve as channels for the diffusions of the ions (the thermochemical radii of CO_3^{2-}, Na^+ and NH_4^+ are 1.78, 0.97, and 1.43 Å, respectively)[20, 21]. On the other hand, the classical mode of crystal growth is also possible. In the production of $NaY(CO_3)_2 \cdot 6H_2O$, the reactions may proceed as follows:

$$Y_2(CO_3)_3 \cdot 2H_2O \rightarrow 2Y^{3+} + 3CO_3^{2-} + 2H_2O \quad (3),$$

$$Y^{3+} + Na^+ + 2CO_3^{2-} + 6H_2O \rightarrow NaY(CO_3)_2 \cdot 6H_2O \quad (4).$$

Similar processes are expected for the production of $(NH_4)Y(CO_3)_2 \cdot H_2O$. For this mode of growth, due to the presence of excess CO_3^{2-}, the amount of aqueous Y^{3+} will play a key role. Supposed that the aqueous Y^{3+} and CO_3^{2-} groups (where the initial concentration of HCO_3^- is ~1/3 M in the mixed solution) are in equilibrium with the $Y_2(CO_3)_3 \cdot 2H_2O$ suspensions, then the concentration of Y^{3+} is calculated to be ~ 4.1×10^{-8} M (Extended Data "Calculation of the Equilibrium Concentration of Y^{3+}"). Such a small amount of Y^{3+} will be quickly consumed by the reaction (4).

To maintain the solubility equilibrium, the Y atoms of the $Y_2(CO_3)_3{\cdot}2H_2O$ suspensions are forced to diffuse into the solution. Hence, the above two growth modes are competing processes for the formation of yttrium double carbonates.

It can be revealed that which process is predominant by comparing the corresponding rate constant *K*, as described by the Arrhenius equation: $K = Ae^{-E_a/(k_BT)}$, where *A* is the frequency factor, E_a is the activation energy, k_B is the Boltzmann constant and *T* is the temperature. For a given system, the activation energy E_a plays a key role in the kinetics of chemical reaction. We have performed first-principles calculations to get the value of E_a in each process. Details of the calculations are summarized in the Methods section. The obtained relative energies regarding the diffusion of CO_3^{2-} , Na^+, NH_4^+, and Y_3^+ along the [100] direction of $Y_2(CO_3)_3{\cdot}2H_2O$ crystal are shown in Fig. 5, together with some intermediate atomic configurations (labeled by capital letters).

As seen in Fig. 5, the diffusion of CO_3^{2-} from surface (A) to the interior (D) of $Y_2(CO_3)_3{\cdot}2H_2O$ involves the surmounting of several barriers: Configurations U_1 → U_2 (E_{a1} = 0.65 eV); B → C (E_{a2} = 0.88 eV); U_3 → U_4 (E_{a3} = 0.29 eV). The other configuration transitions are spontaneous processes. Whereas, Na^+ can easily move into the $Y_2(CO_3)_3{\cdot}2H_2O$ crystal via the nanochannel at a depth of ~ 3.5 Å due to the small barrier (E_{a4} ~ 0.14 eV, E → F). Then they face a transition barrier (F → G, E_{a5} ~ 1.35 eV) of prior arriving at H. The diffusion of NH_4^+ needs to overcome a first barrier E_{a6} (~ 0.49 eV, I → V), and then a second E_{a7} (~ 1.06 eV, J → K), before reaching L. In contrast, the diffusion of Y^{3+} from the interior (M) to the surface (P) needs to overcome an uphill barrier E_{a8} (~ 1.33 eV).

To a multistep diffusion, the averaged rate constant *K* satisfies the relation: $\frac{1}{K} = \sum_{i=1}^{n} \frac{1}{K_i}$, where K_i is the rate constant of step *i* (Extended Data "Calculation of Rate Constant for a Multistep Diffusion" and Fig. 12). With the calculated energy barriers, we can estimate the rate constant for the diffusion process by assuming that the frequency factor *A* to be ~ 10^{12} s^{-1} (ref[22, 23]). The value of *K* turns out to be 4.8×10^{-2} s^{-1}, 3.7×10^{-9} s^{-1}, 9.1×10^{-5} s^{-1}, and 7.4×10^{-9} s^{-1}, for the diffusion of CO_3^{2-}, Na^+, NH_4^+ and Y^{3+}, respectively. It should be noted that the calculations have not taken into account the interactions between CO_3^{2-} and Na^+ or NH_4^+. For Na^+ and NH_4^+, the diffusion from surface to the near surface region with a depth of ~ 2.5 Å takes place easily, with a rate constant of K_4 = 7.6×10^9 s^{-1} (E → F) and K_6 = 3.8×10^4 s^{-1} (I → J), respectively. The accumulation of net charges at the suspended particles will induce another driving force for the crystallization, as predicted by previous work at the H_2O/NaCl system[24]. In our case, the accumulation of Na^+ or NH_4^+ will attract CO_3^{2-} to diffuse into $Y_2(CO_3)_3{\cdot}2H_2O$ by lowering the barrier (E_{a1}, E_{a2}) and thus increase the rate constant for the diffusion. The presence of CO_3^{2-} at the neighboring nanochannels of $Y_2(CO_3)_3{\cdot}2H_2O$ will in turn help the Na^+ or NH_4^+ to overcome the rate-determining barrier (E_{a5} for Na^+ and E_{a7} for NH_4^+) to reach the more stable energy configurations. For configurations near the surface (Extended Data Fig. 13), we have calculated the strength of electrostatic attraction of CO_3^{2-} — Na^+ to be ~ 1.96 eV, and CO_3^{2-} — NH_4^+ to be ~ 2.27 eV. On the contrary, there is no such positive feedback effects in the diffusion of Y^{3+} from

inside $Y_2(CO_3)_3{\cdot}2H_2O$ to the surface, due to the screening effect of the coordination CO_3^{2-} groups around each Y^{3+}.

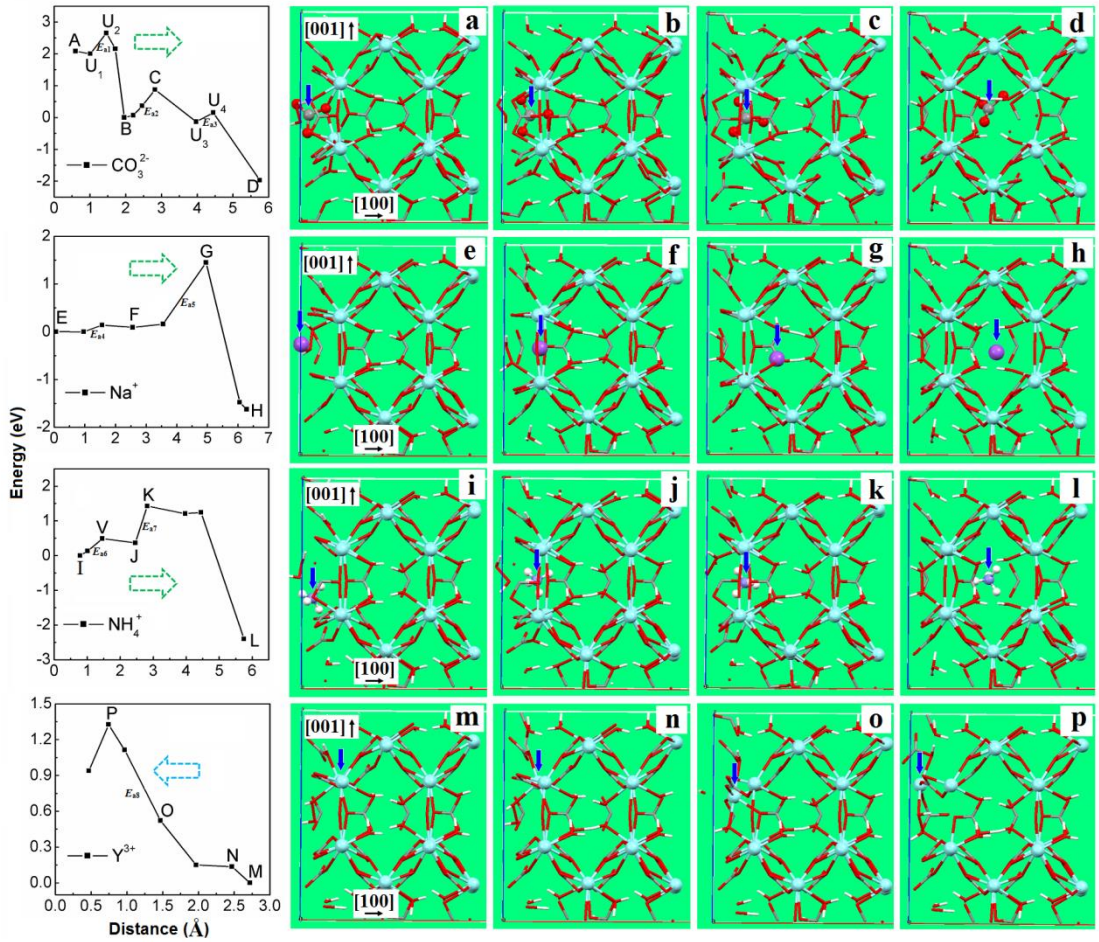

Figure 5 | Energetics and atomic configurations regarding the diffusion of atoms. Left panels: Relative energies of the atomic configurations as a function of the distance to the (100) surface of $Y_2(CO_3)_3{\cdot}2H_2O$. The configurations are located on the diffusion pathway for the atoms from surface to the interior (CO_3^{2-}, Na^+, NH_4^+), or from the interior to surface (Y^{3+}), with the direction of diffusion schematically indicated by dashed arrows. For CO_3^{2-} and NH_4^+, the distance is measured from the geometry center of the group to the surface. **Right panels:** Atomistic structures for some typical configurations, where the labeling lowercase letters **a-p** have a one-to-one correspondence to the energy configurations marked by the capital letters **A-P** in the left panels. For clear illustration, the Y^{3+} atoms (sky blue) and the atoms/groups (indicated by vertical arrows) are represented by small balls (gray for C, purple for Na and violet for N), while other atoms are represented by capped sticks in different colors: red for O and white for H.

The analysis above naturally points to the conclusion that it is the intercalation reaction instead of the classical mode of growth (dissolution-nucleation) that plays a dominant role in the

formation of yttrium double carbonates. Variation of the frequency factor *A* by one order of magnitude will not change the conclusion. Supposed that the contribution of classical mode of growth is not negligible, then the least time required for the formation of yttrium double carbonates is the order of 10^8 s (~ 10^3 days), which is well beyond the time scale of the present experiment (1 - 2 hours).

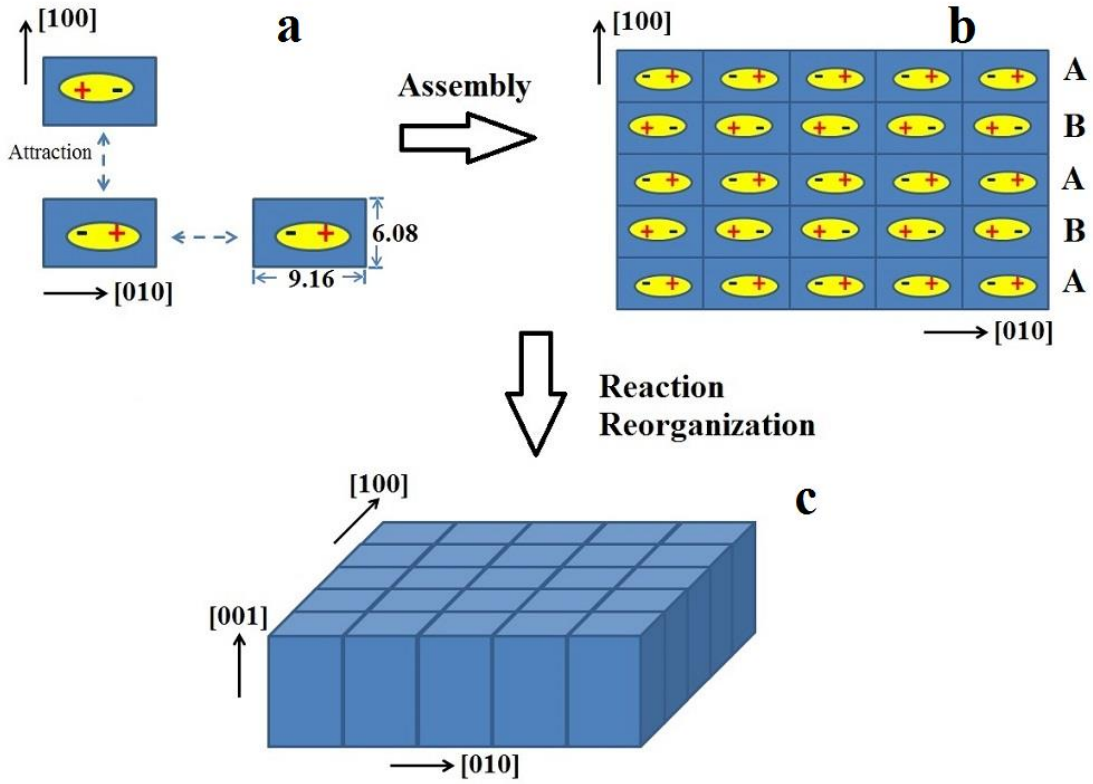

Figure 6 | Schematic diagram for the chemical reaction directed OA in yttrium double carbonates. a, Dipole-dipole interactions viewed from [001] direction. **b,** Oriented assembly of the nanoparticles via electrostatic interactions. **c,** Formation of the 2D-like sheets by reaction and position reorganization of the atoms.

It is fascinating how the suspended particles with intercalated ions are assembled to form the single-crystalline, 2D-like sheets obtained in our experiments. Besides the stresses associated with lattice mismatch, which tend to induce rotation of the nanoparticles to contact at surfaces with the same orientation[9,25] and to form aligned configurations, the most important driving force is the electrostatic interactions between nanoparticles. Judging from the rate constant, the Na^+ (NH_4^+) ions will enter one nanochannel firstly and then followed by the CO_3^{2-} that will diffuse into the neighboring nanochannel. The interactions between Na^+ (NH_4^+) and CO_3^{2-} help the ions surmount the energy barrier and arrive at the stable sites. To maintain charge neutrality, one more Na^+ (NH_4^+) will be attracted into the nanochannel where CO_3^{2-} resides. Consequently, the two neighboring nanochannels will contain net charges with the same absolute value but opposite

signs (±1). This forms an electric dipole. Figure 6 schematically shows the OA process of the nanoparticles via dipole-diploe interactions. The distances between the dipoles are determined by the dimension of the unit cell of $Y_2(CO_3)_3 \cdot 2H_2O$, which is ~ 6.08 Å, 9.16 Å, 15.11 Å[17] in the X, Y, Z direction, respectively. Since the strength of dipole-dipole interaction decreases with r^3 (r: the dipole-diploe separation), the interactions in the Z direction will be much weaker than in the X & Y directions. Therefore, the assembly of the nanoparticles will proceeds mainly along X and Y directions while the packing along the Z direction will be much slower. This picture holds for the alignment of nanoparticles which contain a number of unit cells, since the dominant dipole-dipole interactions along each direction are still determined by the lattice constants. As shown in Fig. 6, the Coulomb interactions between the nanoparticles will result in an ABAB stacking order in the X ([100]) direction, where the B lines are just rotated by 180° from A lines. Reaction and reorganization (details at atomic level are left for future studies) of the atoms in the assembled units will lead to the fusion of the interfaces of crystallites and get the final products: the 2D-like sheets (Fig. 3d).

In summary, by combining experimental and theoretical efforts, we demonstrate that with the participation of $NaHCO_3$ and NH_4HCO_3, micron-sized sheets of $NaY(CO_3)_2 \cdot 6H_2O$ and $(NH_4)Y(CO_3)_2 \cdot H_2O$ can be formed from $Y_2(CO_3)_3 \cdot 2H_2O$ nanoparticles through a chemical reaction directed oriented attachment. In contrast to conventional OA process, this OA growth can produce new single-crystalline substances whose crystallographic structures and chemical constituents are different (usually more complicated) from that of the precursor nanoparticles. Such an OA mechanism shows applicability in a number of salts. Our findings not only extend the territory of the nonclassical aggregation-based crystal growth mode, but also provide a feasible approach for creating new functional materials with complex architectures from simple nanoparticles.

METHODS SUMMARY

Nanoparticles synthesis and oriented attachment. Several groups of $Y_2(CO_3)_3 \cdot 2H_2O$ nanoparticle suspensions were synthesized first by dripping aqueous NH_4HCO_3 solution (1.0 M, 10 ml) slowly into the mixed solution (20 ml, pre-heating at 60 ℃) of $Y(NO_3)_3$ (0.2 M) and $(NH_4)_2SO_4$ (0.01 M) with stirring. Afterwards, aqueous solutions (1.0 M, 15 ml) of $NaHCO_3$, NH_4HCO_3, NaOH, and NH_4OH were dripped into the above $Y_2(CO_3)_3 \cdot 2H_2O$ suspension at a rate of 1 ml/min under vigorous agitation, respectively. After reaction for 10-120 min, the white products (labeled as Y1, Y2, Y3, and Y4, respectively) were harvested and washed thoroughly with deionized water and absolute ethyl alcohol successively. The similar procedure was also used for the preparation of $NaGd(CO_3)_2 \cdot 6H_2O$ and $KNd(CO_3)_2 \cdot xH_2O$ micron-sized sheets.

Post-treatment to the micron-sized sheets. Typically, $(NH_4)Y(CO_3)_2 \cdot H_2O$ suspensions (3 ml) were mixed with 3 ml NH_4OH solution (1.0 M) into 45 ml of solvents (ionized water, absolute ethyl alcohol, and toluene, respectively). The obtained mixtures were then aged at 160 ℃ for 24 hrs in a Teflon autoclave (65 ml) respectively.

Characterization. The particle size distribution of $Y_2(CO_3)_3 \cdot 2H_2O$ nanoparticles was measured by small angle X-ray scattering (SAXS, Philips X'Pert Pro MPD). The phase, microstructure, and morphology of the products were investigated using X-ray diffraction (XRD, Philips X'pert, $Cu_{k\alpha}$), field-emission scanning electron microscopy (FESEM, Sirion 200), transmission electron microscopy (TEM, JEM-2010), and tapping-mode atomic force microscopy (AFM, Seiko, SPA-300HV & SPI3800N), respectively. The yttrium content of $(NH_4)Y(CO_3)_2 \cdot H_2O$ micron-sized sheets was analyzed by inductively coupled plasma emission spectrometer (ICP, Thermal Electron). Carbon, Hydrogen, and Nitrogen contents of $(NH_4)Y(CO_3)_2 \cdot H_2O$ micron-sized sheets were determined by an elemental analyzer (Vario EL cube, Elementar). Fourier transform infrared (FTIR) spectroscopy of the samples was accomplished using a Nexus Nicolet spectrometer.

First-principles calculations. Our first-principles calculations are carried out by the Vienna *ab initio* simulation package (VASP)[26,27], which is based on density functional theory (DFT). A plane wave basis set and the projector-augmented-wave (PAW) potentials[28,29] are employed to describe the electron-ion interactions. The exchange-correlation interactions of electrons are described by the PBE functional[30]. The energy cutoff for plane waves is 600 eV. The primitive cell of crystalline $Y_2(CO_3)_3 \cdot 2H_2O$ is constructed based on the experimental work[17], which consists of 4 formula units of $Y_2(CO_3)_3 \cdot 2H_2O$. To simulate the diffusion of atoms (from surface to interior (CO_3^{2-}, Na^+, NH_4^+) or interior to surface (Y^{3+})), we take a (2×1×1) unit cell (totally 160 atoms) to model the $Y_2(CO_3)_3 \cdot 2H_2O$ nanoparticles, with the (100) surface separated by a vacuum layer of ~ 10 Å. The diffusion of atoms take place along the [100] direction, the direction of the nanochannel in $Y_2(CO_3)_3 \cdot 2H_2O$. A 1×2×1 k-mesh generated using the Monkhorst-Pack scheme[31] is employed for all the calculations. The aqueous environment surrounding the $Y_2(CO_3)_3 \cdot 2H_2O$ nanoparticles is not considered in our simulation due to the following two reasons: i) The diffusion of atoms in liquids is much faster/easier than in solids; and ii) The inclusion of liquid water is too much demanding for the present first-principles simulations.

References

1. Zhang, Q., Liu, S.-J. & Yu, S.-H. Recent advances in oriented attachment growth and synthesis of functional materials: concept, evidence, mechanism, and future. *J. Mater. Chem.* **19**, 191-207 (2009).

2. Banfield, J. F., Welch, S. A., Zhang, H. Z., Ebert, T. T. & Penn, R. L. Aggregation-based crystal growth and microstructure development in natural iron oxyhydroxide biomineralization products. *Science* **289**, 751-754 (2000).
3. Penn, R. L. & Banfield, J. F. Imperfect oriented attachment: Dislocation generation in defect-free nanocrystals. *Science* **281**, 969-971 (1998).
4. Zhang, J., Huang, F. & Lin, Z. Progress of nanocrystalline growth kinetics based on oriented attachment. *Nanoscale* **2**, 18-34 (2010).
5. Burrows, N. D., Hale, C. R. H. & Penn, R. L. Effect of Ionic Strength on the Kinetics of Crystal Growth by Oriented Aggregation. *Crystal Growth & Design* **12**, 4787-4797, doi:10.1021/cg3004849 (2012).
6. Zhang, D.-F., Sun, L.-D., Yin, J.-L., Yan, C.-H. & Wang, R.-M. Attachment-Driven Morphology Evolvement of Rectangular ZnO Nanowires. *The Journal of Physical Chemistry B* **109**, 8786-8790, doi:10.1021/jp050631l (2005).
7. Huang, F., Zhang, H. Z. & Banfield, J. F. The role of oriented attachment crystal growth in hydrothermal coarsening of nanocrystalline ZnS. *J. Phys. Chem. B* **107**, 10470-10475, doi:10.1021/jp035518e (2003).
8. Schliehe, C. *et al.* Ultrathin PbS Sheets by Two-Dimensional Oriented Attachment. *Science* **329**, 550-553, doi:10.1126/science.1188035 (2010).
9. Cölfen, H. & Mann, S. Higher-order organization by mesoscale self-assembly and transformation of hybrid nanostructures. *Angew. Chem. Int. Ed.* **42**, 2350-2365, doi:10.1002/anie.200200562 (2003).
10. Niederberger, M. & Colfen, H. Oriented attachment and mesocrystals: Non-classical crystallization mechanisms based on nanoparticle assembly. *Phys. Chem. Chem. Phys.* **8**, 3271-3287, doi:10.1039/b604589h (2006).
11. Cho, K. S., Talapin, D. V., Gaschler, W. & Murray, C. B. Designing PbSe nanowires and nanorings through oriented attachment of nanoparticles. *J. Am. Chem. Soc.* **127**, 7140-7147, doi:10.1021/ja050107s (2005).
12. Saito, N., Matsuda, S. & Ikegami, T. Fabrication of transparent yttria ceramics at low temperature using carbonate-derived powder. *J. Am. Ceram. Soc.* **81**, 2023-2028 (1998).
13. Sun, X., Dong, S. & Wang, E. High-Yield Synthesis of Large Single-Crystalline Gold Nanoplates through a Polyamine Process. *Langmuir* **21**, 4710-4712, doi:10.1021/la047267m (2005).
14. Sangwal, K. Growth kinetics and surface morphology of crystals grown from solutions: Recent observations and their interpretations. *Prog. Cryst. Growth Charact. Mater.* **36**, 163-248, doi:10.1016/s0960-8974(98)00009-6 (1998).
15. Dalmaschio, C. J., Ribeiro, C. & Leite, E. R. Impact of the colloidal state on the oriented attachment growth mechanism. *Nanoscale* **2**, 2336-2345 (2010).
16. Yu, J. H. *et al.* Synthesis of quantum-sized cubic ZnS nanorods by the oriented attachment mechanism. *J. Am. Chem. Soc.* **127**, 5662-5670, doi:10.1021/ja044593f (2005).
17. Miyawaki, R., Kuriyama, J. & Nakai, I. The redefinition of tengerite-(Y), Y2(CO3)3.2-3H2O, and its crystal-structure *Am. Mineral.* **78**, 425-432 (1993).
18. Grice, J. D., Gault, R. A., Roberts, A. C. & Cooper, M. A. Adamsite-(Y), a new sodium–yttrium carbonate mineral species from Mont Saint-Hilaire, Quebec. *The Canadian Mineralogist* **38**, 1457-1466, doi:10.2113/gscanmin.38.6.1457 (2000).
19. Firsching, F. H. & Mohammadzadei, J. Solubility products of the rare-earth carbonates. *Journal of Chemical & Engineering Data* **31**, 40-42, doi:10.1021/je00043a013 (1986).
20. Renard, F., Montes-Hernandez, G., Ruiz-Agudo, E. & Putnis, C. V. Selenium incorporation into calcite and its effect on crystal growth: An atomic force microscopy study. *Chem. Geol.* **340**, 151-161, doi:10.1016/j.chemgeo.2012.12.017 (2013).
21. Barker, D. S. Ammonium in alkali feldspars. *Am. Mineral.* **49**, 851-& (1964).
22. Wu, J., Wang, E. G., Varga, K., Liu, B. G., Pantelides, S. T., and Zhang, Z. Island Shape Selection in Pt(111) Submonolayer Homoepitaxy with or without CO as an Adsorbate. *Phys. Rev. Lett.* **89**, 146103 (2002).
23. Lazauskas, T., Kenny, S. D. and Smith, R. Influence of the prefactor to defect motion in α-Iron during long time scale simulations. *J. Phys.*: *Condens. Matter* **26**, 395007 (2014).
24. Yang, Y. and Meng, S. Atomistic nature of NaCl nucleation at the solid-liquid interface. *J. Chem. Phys.* **126**, 044708 (2007).
25. van Huis, M. A. *et al.*, Low-Temperature Nanocrystal Unification through Rotations and Relaxations Probed by in Situ Transmission Electron Microscopy. *Nano Lett.* **8**, 3959-3963, doi:10.1021/nl8024467 (2008).
26. Kresse, G. and Hafner, J. Ab initio molecular dynamics for liquid metals. *Phys. Rev. B* **47**, 558 (1993).
27. Kresse, G. and Furthmüller, J. Efficient iterative schemes for ab initio total-energy calculations using a plane-wave basis set. *Phys. Rev. B* **54**, 11169 (1996).
28. P. E. Blöchl, Projector augmented-wave method. *Phys. Rev. B* **50**, 17953 (1994).
29. Kresse, G. and Joubert, D. From ultrasoft pseudopotentials to the projector augmented-wave method. *Phys. Rev. B* **59**, 1758 (1999).
30. Perdew, J. P., Burke, K., Ernzerhof, M. Generalized Gradient Approximation Made Simple. *Phys. Rev. Lett.* **77**, 3865 (1996).
31. Monkhorst, H. J. and Pack, J. D. Special points for Brillouin-zone integrations. *Phys. Rev. B* **13**, 5188 (1976).

Acknowledgements

This work was supported in part by National Natural Science Foundation of China (No. 11374306, No. 11174292, No. 50972146, and No. 10904144). The authors thank Professor Lide Zhang and Guowen Meng for helpful discussions; Professor Xiaojia Chen for reading of the manuscript; Li Chen and Zhaoqin Chu for their help with SAXS and TEM analyses. Y. F. Liu is grateful to Dr. Junming Xu, Zhen Gu and Hualing Ding for helpful reference and discussion. The DFT simulations are performed using the supercomputers of the Hefei Branch of Supercomputing Center of Chinese Academy of Sciences; the supercomputers of the Institute for Materials Research, Tohoku University; and the Tian He II series supercomputers. Y.Y. acknowledges support from the National Natural Science Foundation of China (No. 11474285).

Author contributions

Y.F.L. designed and performed the experiments. Y.F.L. and X.G.Z processed TEM data. Y.F.L., Z.F.D. and C.J.S. contributed to the FESEM and AFM analyses. H.X.X., D.L., and J.Z. processed XRD and FTIR data. Y.F.L. contributed to the element analysis and drew the schematic drawings. Y.F.L., Y.Y. and X.Y.Q. wrote the manuscript. X.Y.Q. directed the experimental research. Y.Y., Z.Z. and Y.K. provide the theoretical support. Y.Y. conceived the theoretical model and performed the DFT calculations. All authors contribute to discussions.

Author Information

The authors declare no competing financial interests. Readers are welcome to comment on the online version of the paper. Correspondence and requests for materials should be addressed to X.Y.Q (xyqin@issp.ac.cn), Y.F.L. (liuyongfei.mse@gmail.com), and Y.Y. (yyang@theory.issp.ac.cn; yyangtaoism@gmail.com).

Online Content Additional Extended Data and Discussions and Calculations are available in the online version of this paper; references unique to these sections appear only in the online paper.

Extended Data Figures, Discussions and Calculations

This supplementary file includes:

Extended Data Figures 1 to 16

Extended Data Table 1

Additional Discussions and Calculations.

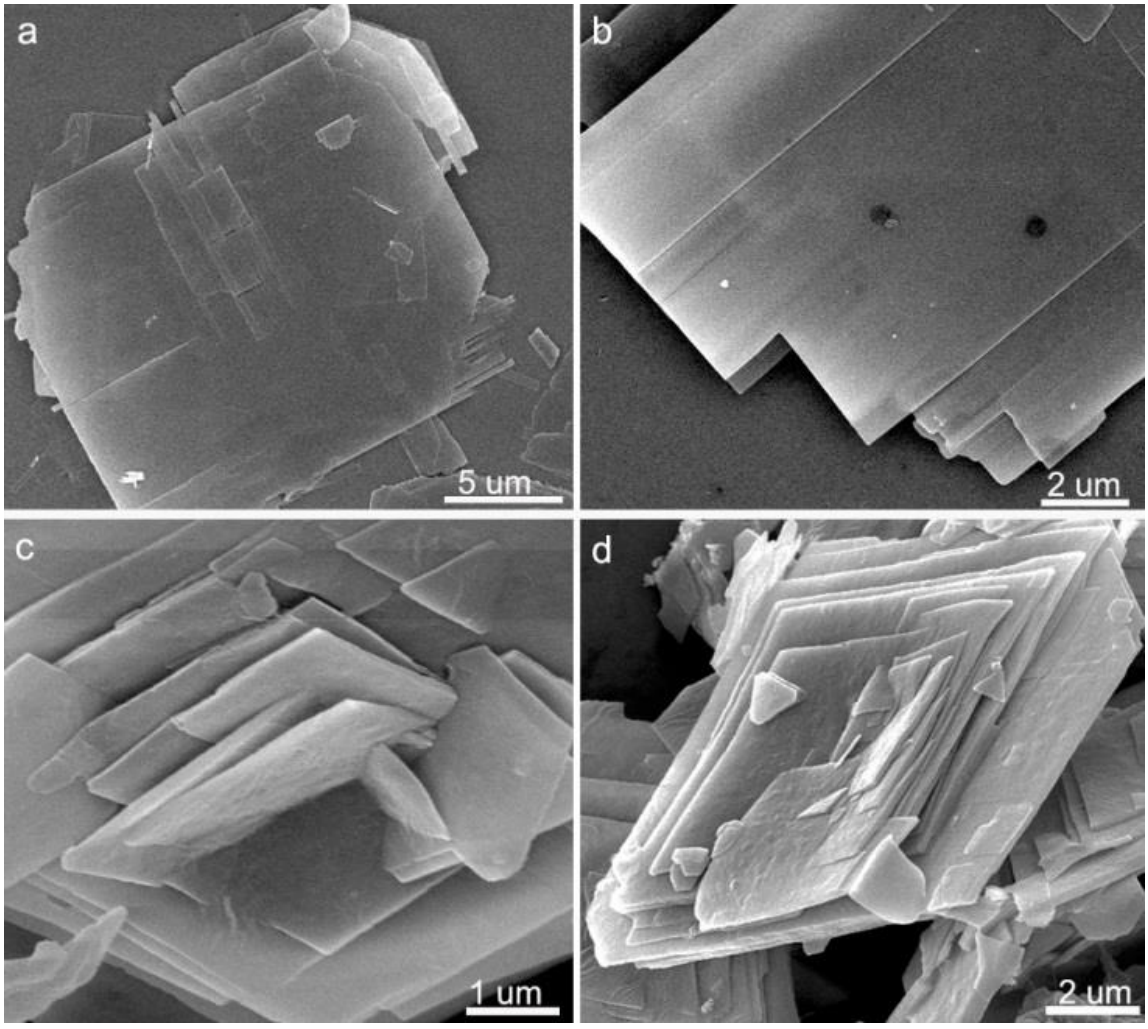

Extended Data Figure 1 | FESEM images of the obtained sheets. (a-b) $NaY(CO_3)_2\ 6H_2O$, (c-d) $(NH_4)Y(CO_3)_2\ H_2O$.

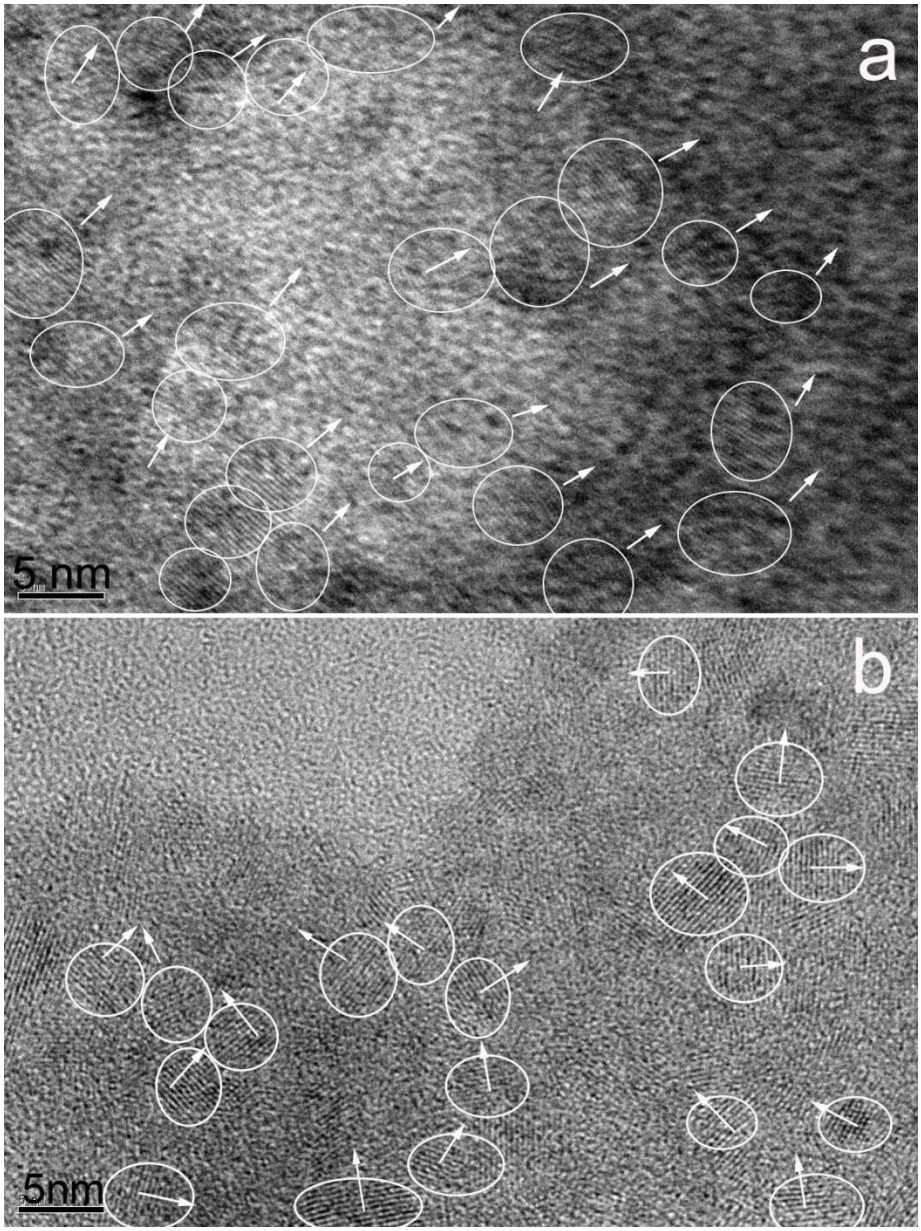

Extended Data Figure 2 | High resolution TEM images of the $NaY(CO_3)_2 \cdot 6H_2O$ sheets (a) and precursor $Y_2(CO_3)_3 \cdot 2H_2O$ particles (b).

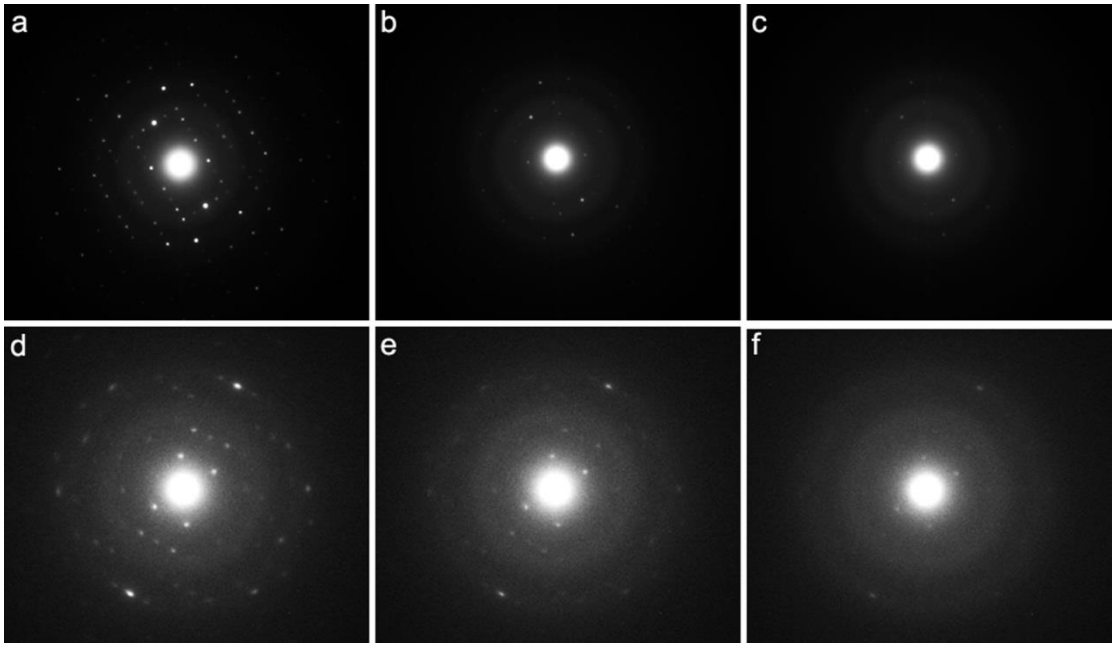

Extended Data Figure 3 | Evolution of SAED patterns of (a-c) $NaY(CO_3)_2\ 6H_2O$ sheet within ~ 30 seconds and (d-f) $(NH_4)Y(CO_3)_2\ H_2O$ sheet within ~ 10 seconds due to the beam damage. Such rapid decomposition of $(NH_4)Y(CO_3)_2\ H_2O$ sheet leads to difficulty to obtain the lattice-fringe image.

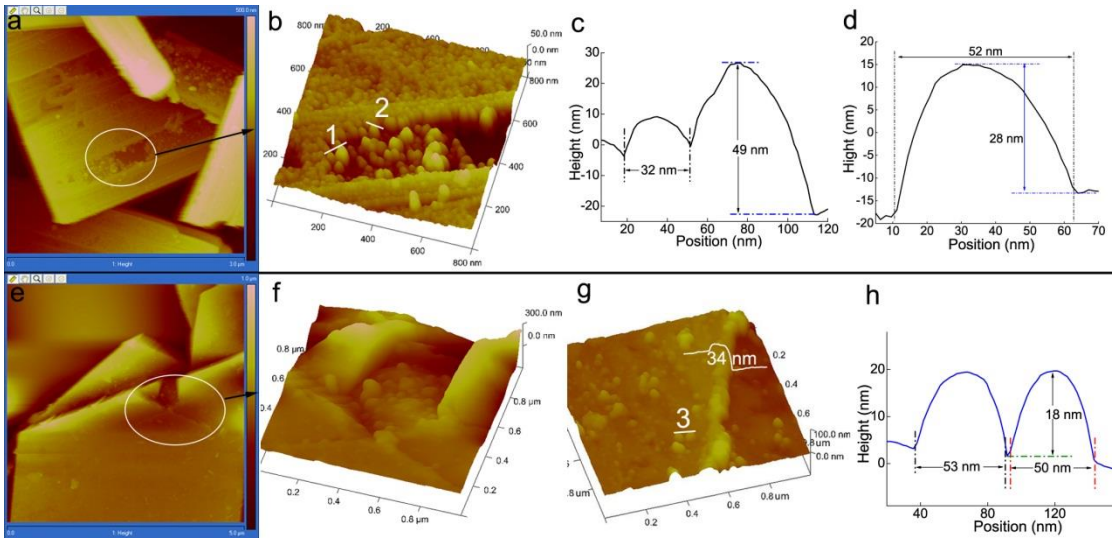

Extended Data Figure 4 | AFM images of the obtained $NaY(CO_3)_2\ 6H_2O$ (a) and $(NH_4)Y(CO_3)_2\ H_2O$ (e) sheets. (b) 3D AFM surface plot of the defective area for $NaY(CO_3)_2\ 6H_2O$ sheet marked in (a). (c, d) Cross-sectional analyses of the sites marked as 1 and 2 in (b), respectively. (f, g) 3D AFM surface plots of step site for $(NH_4)Y(CO_3)_2\ H_2O$ sheets marked in (e). (h) Cross-sectional analysis of the sites marked as 3 in (g).

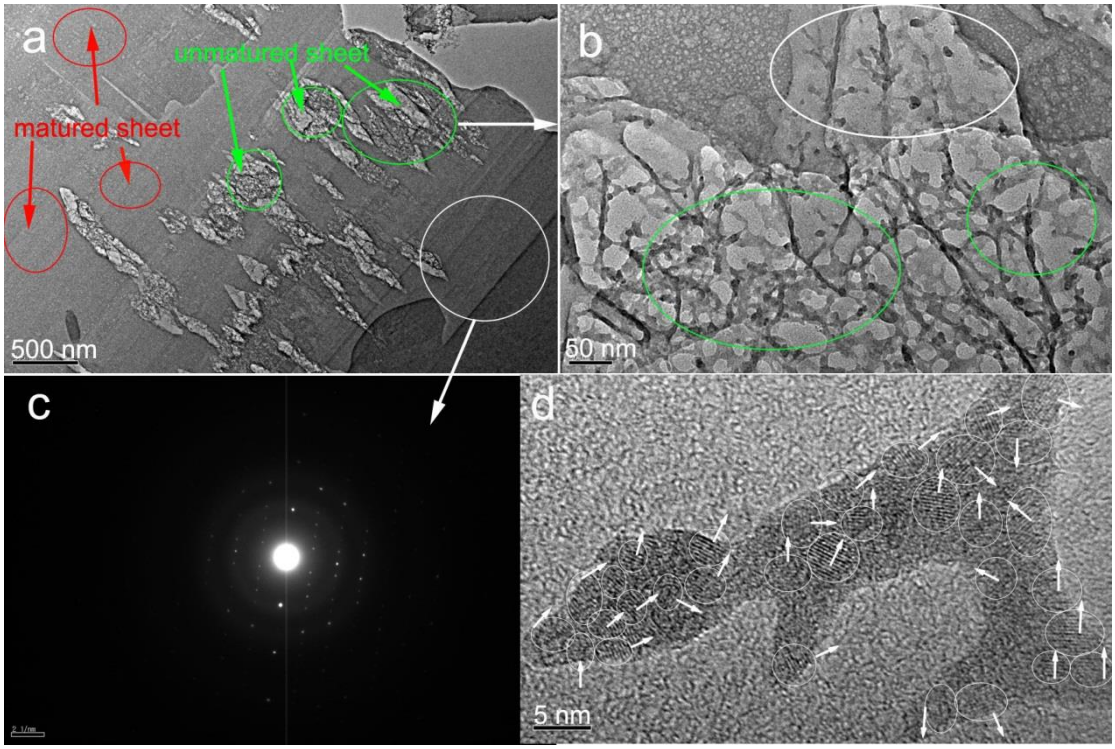

Extended Data Figure 5 | TEM images (a and b), SAED pattern (c), and HRTEM image (d) for the intermediates in the formation of $NaY(CO_3)_2\ 6H_2O$ sheets.

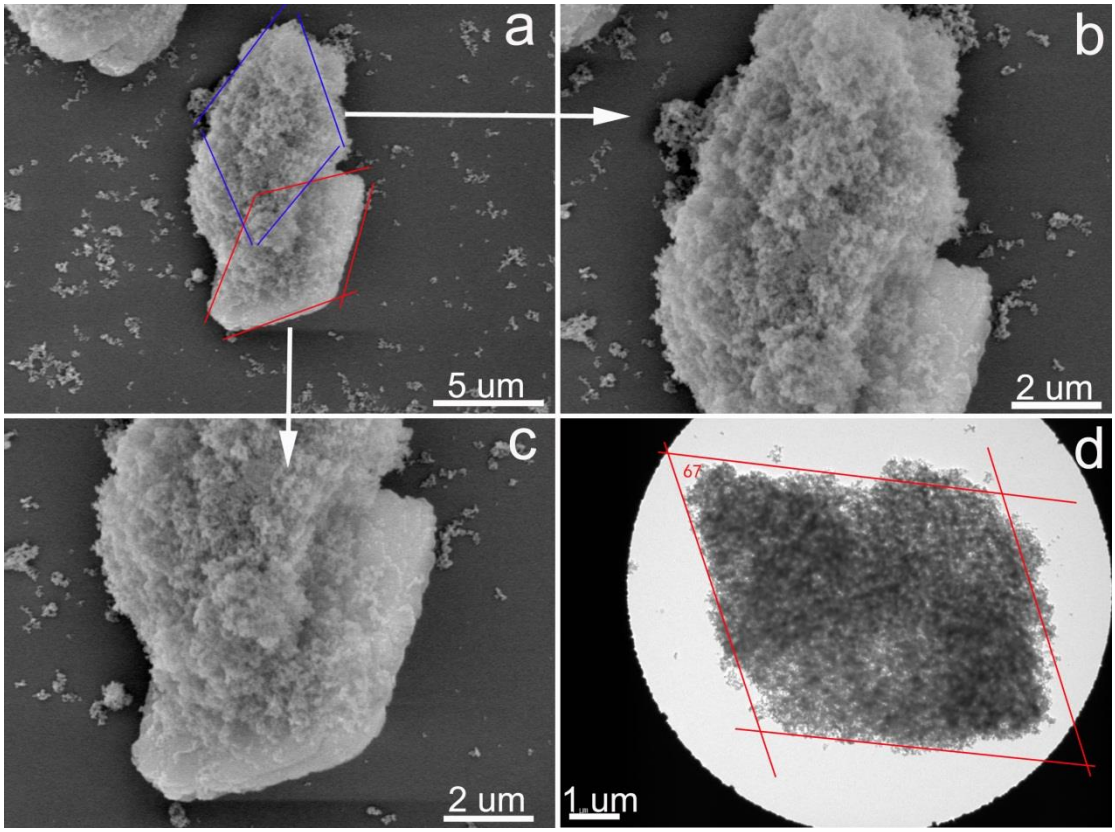

Extended Data Figure 6 | FESEM (a-c) and TEM (d) images for the intermediates in the formation of $(NH_4)Y(CO_3)_2 \cdot H_2O$ sheets.

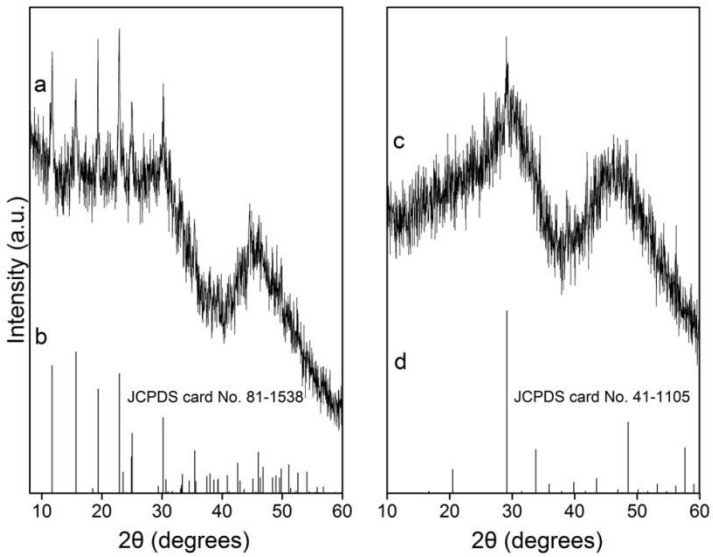

Extended Data Figure 7 | XRD patterns of the $(NH_4)Y(CO_3)_2 \cdot H_2O$ sheets after solvothermal treatment in ethanol at 160 ℃ for 4 hrs (a) and 24 hrs (c). Therein (b) is orthorhombic $Y_2(CO_3)_3 \cdot 2H_2O$ pattern (JCPDS No. 81-1538) and (d) is cubic Y_2O_3 pattern (JCPDS No. 41-1105).

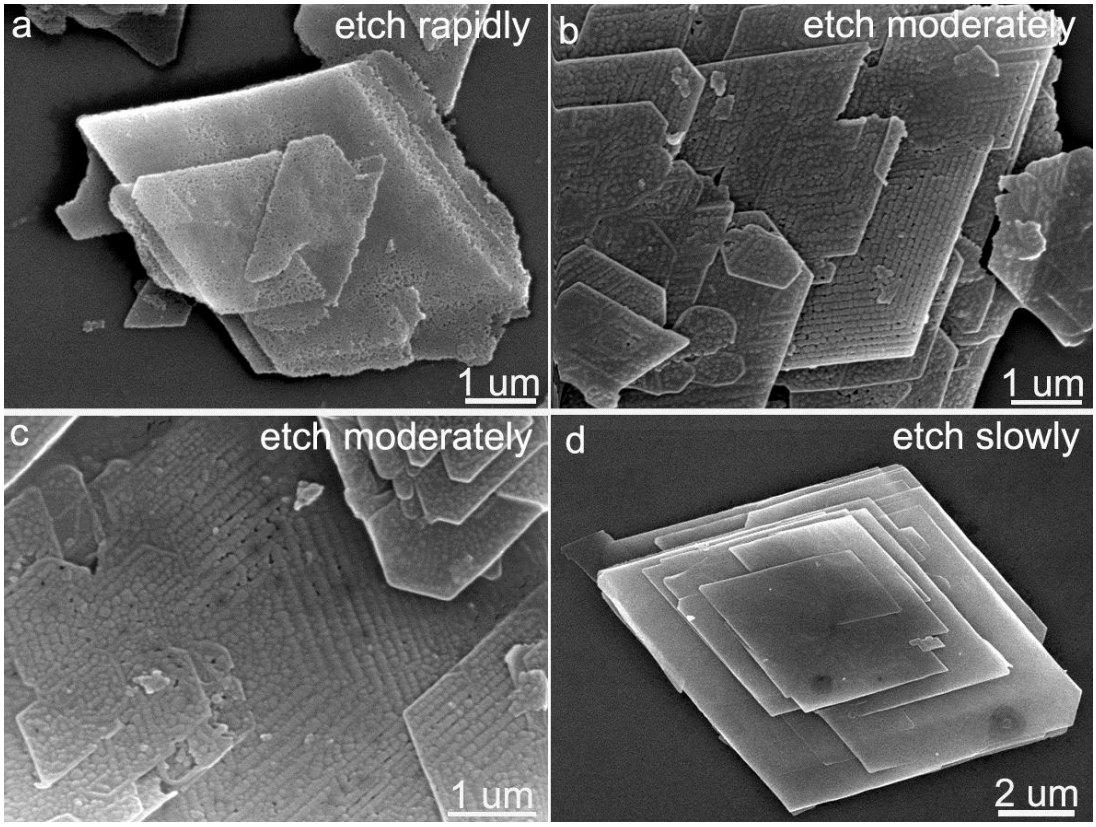

Extended Data Figure 8 | FESEM images of the $(NH_4)\cdot Y(CO_3)_2\cdot H_2O$ sheets after solvothermal treatment at 160 ℃ for 24 hrs in ethanol with different addition of $NH_3\cdot H_2O$: 0 mL (a), 3 mL (b and c), and 6 mL (d).

As the XRD examination revealed (Extended Data Fig. 7), during the solvothermal etching treatment of the $(NH_4)\cdot Y(CO_3)_2\cdot H_2O$ sheets, following chemical reactions will occur:

$$2(NH_4)Y(CO_3)_2\cdot H_2O \rightarrow Y_2(CO_3)_3\cdot 2H_2O + 2NH_4^+ + CO_3^{2-} \quad (5)$$

$$Y_2(CO_3)_3\cdot 2H_2O \rightarrow Y_2O_3 + 3CO_2 + 2H_2O \quad (6)$$

Theoretically, the reaction will take place easily in the defect-rich interface regions. In order to make the defect-rich regions show up clearly, a moderate reaction is required to insure that reaction (5) occurs at these regions preferentially. The chemical reaction was tuned by altering the addition of $NH_3\bullet H_2O$ (supplying NH_4^+), which can decelerate the decomposition reaction by increasing the concentration of NH_4^+ to accelerate the reverse reaction of (5). As shown in Extended Data Fig. 8, with increasing addition of $NH_3\bullet H_2O$, the dissolution rate slows down gradually, which allow us to obtain the products with disordered wormhole-like porous structure, the products with regular particle array patterns, and the products with smooth surfaces, respectively. The change trend in the surface morphologies of the etched sheets is in good agreement with our above analysis, showing the validity of the etching.

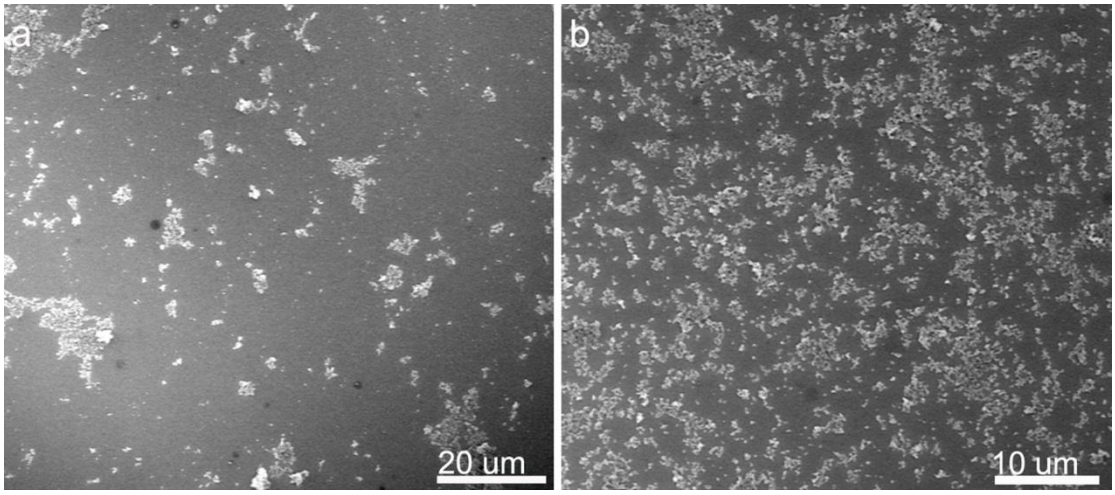

Extended Data Figure 9 | FESEM images of the samples synthesized by introducing (a) NaOH and (b) NH_4OH aqueous solutions into $Y_2(CO_3)_3 \cdot 2H_2O$ nanoparticle suspensions. No micron-sized or nano-sized sheets were obtained, indicating the key role of the double-salt reaction in the OA process.

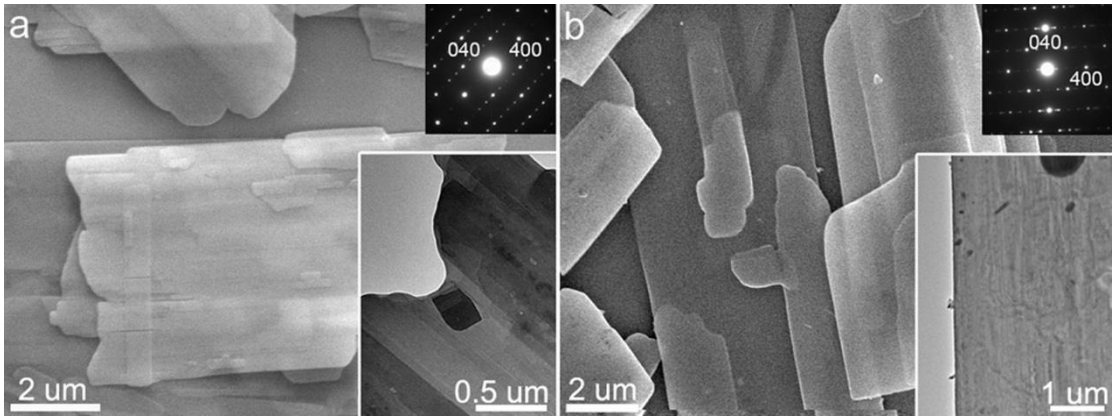

Extended Data Figure 10 | FESEM images of the micron-sized sheets synthesized via the OA process: (a) $NaGd(CO_3)_2 \cdot 6H_2O$ (JCPDS card No. 31-1291); (b) $KNd(CO_3)_2 \cdot xH_2O$. Insets are corresponding TEM images and SEAD patterns. The SAED patterns show single-crystalline nature of the sheets, indicating that the formation of these multilayer sheets is not from the simple and random packing of single-layer sheets, but the result of well-organized layer growth through the OA of nanoparticles. The SAED pattern of $KNd(CO_3)_2 \cdot xH_2O$ is indexed according to the data (Tetragonal, a=13.28 Å, c=10.00 Å) from ref[32].

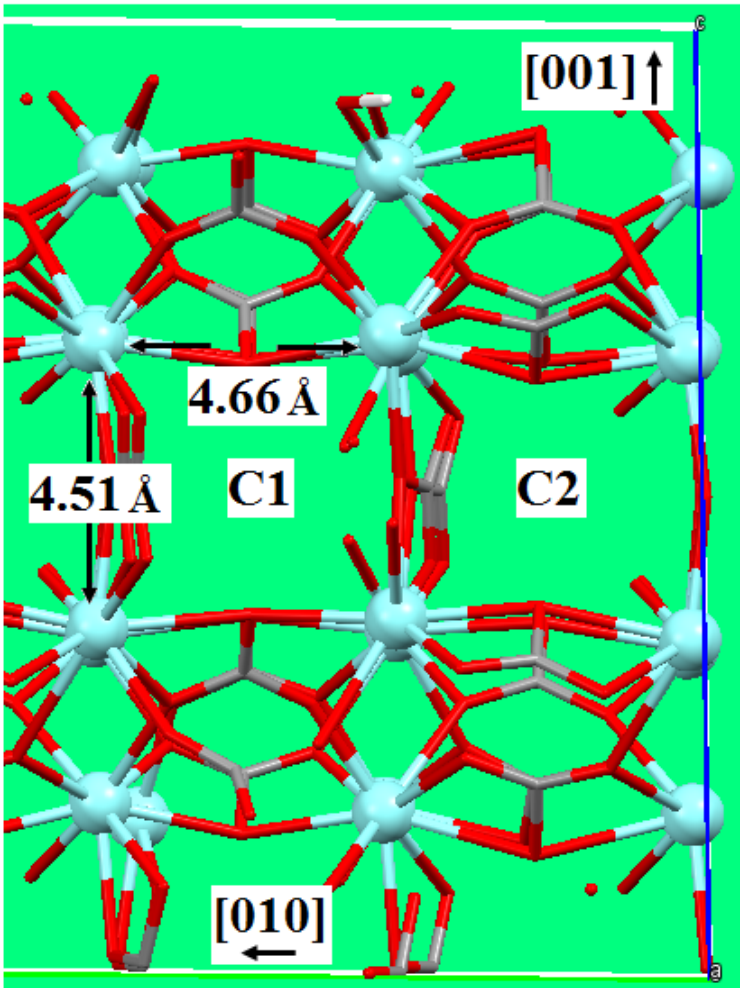

Extended Data Figure 11 | Atomistic structures of the nanochannels (C1 and C2) in $Y_2(CO3)_3 \cdot 2H_2O$ for the diffusion of CO_3^{2-}, Na^+, and NH_4^+.

Calculation of the Equilibrium Concentration of Y^{3+}.

1. The Equilibrium Concentration of CO_3^{2-}

From the preparation procedure (Methods Summary part) the initial concentration of $NaHCO_3$ (NH_4HCO_3) is estimated to ~ 1/3 mol/L (i.e., 1/3 M), then the concentration of HCO_3^- is ~ 1/3 M, due to the fact that $NaHCO_3$ (NH_4HCO_3) is strong electrolyte. The group HCO_3^- is partly dissociated into H^+ and CO_3^{2-} with an equilibrium constant of K ~ 4.7×10^{-11} at 25 ℃[19], it follows that $K = [H^+]\times[CO_3^{2-}]/[HCO_3^-] = [CO_3^{2-}]^2/[HCO_3^-]$. Then, it can be deduced that the equilibrium concentration of CO_3^{2-} , $[CO_3^{2-}] = 3.9\times10^{-6}$ M.

2. The Equilibrium Concentration of Y^{3+}

With the equilibrium concentration of CO_3^{2-} and the solubility product of $Y_2(CO_3)_3$ (K_{sp} = 1.03×10^{-31})[19], one has $K_{sp} = [Y^{3+}]^2\times[CO_3^{2-}]^3$, and consequently $[Y^{3+}] = 4.1\times10^{-8}$ M. This is the equilibrium concentration of Y^{3+} in the solution, before the onset of intercalation reaction.

Calculation of Rate Constant for a Multistep Diffusion. The diffusion of atoms from one atomic configuration to another is equivalent to a chemical reaction in the sense of the breaking of old bonds and the formation of new bonds. The speed of diffusion can be similarly describe by the rate constant: $K = Ae^{-E_a/(k_BT)}$. A multistep diffusion is just similar to a multistep chemical reaction. Consider the multistep diffusion of particle A from the original configuration (labeled by "0") via a number of intermediate configurations (labeled by "1, 2, 3,…, n-1") to the final configuration (labeled by "n") as follows:

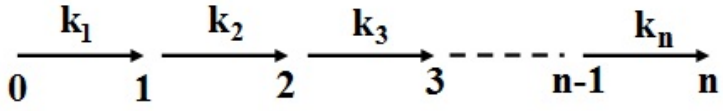

Extended Data Figure 12 | Schematic diagram for a multistep diffusion process with the rate constant k_i for step *i*.

The rate constant is k_1 for the diffusion from configuration 0 to 1, and is k_2 for the diffusion from configuration 1 to 2, and so forth. Given that the amount of substance A is n_A, then the time needed for the diffusion from configuration 0 to configuration *n* is: $t = \frac{n_A}{k_1} + \frac{n_A}{k_2} + \frac{n_A}{k_3} + ... + \frac{n_A}{k_n} = \sum_{i=1}^{n} \frac{n_A}{k_i}$. The average rate constant is $k = \frac{n_A}{t}$, which satisfies the relation: $\frac{1}{k} = \sum_{i=1}^{n} \frac{1}{k_i}$. It follows that the step with the smallest k_i (equivalently, the highest activation energy E_a) plays a major role in determining the value of *k*, which is the so-called rate-determining step[33].

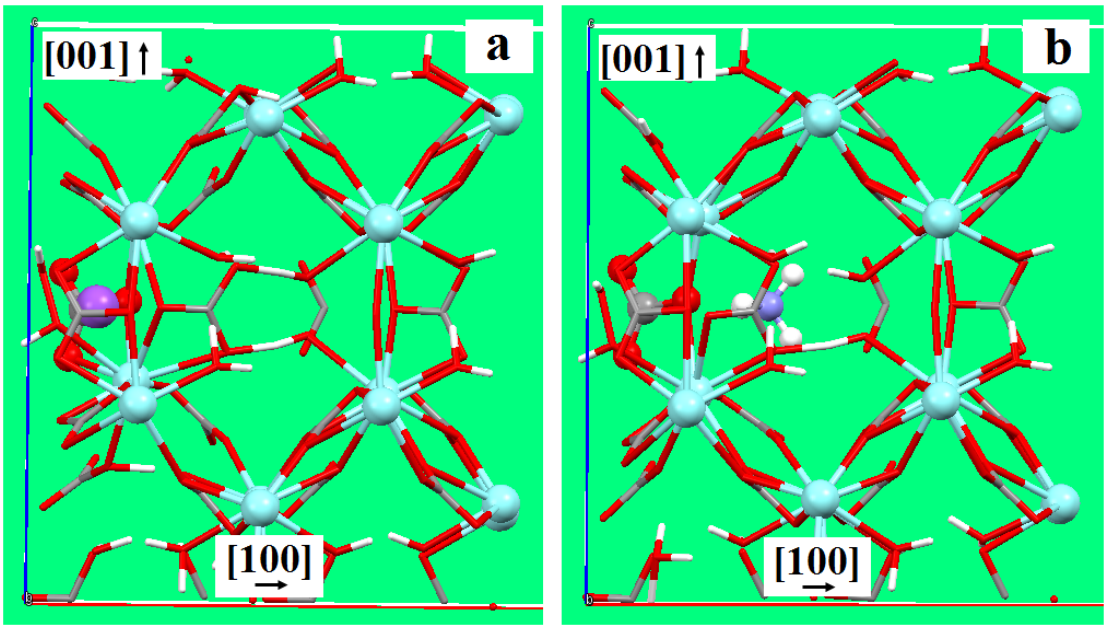

Extended Data Figure 13 | Atomistic models for the calculation of electrostatic interactions. (a). Interaction between CO_3^{2-} and Na^+. (b). Interaction between CO_3^{2-} and NH_4^+. CO_3^{2-} locates near the surface region. The presentations of balls and capped sticks have the same meaning as in Fig. 5.

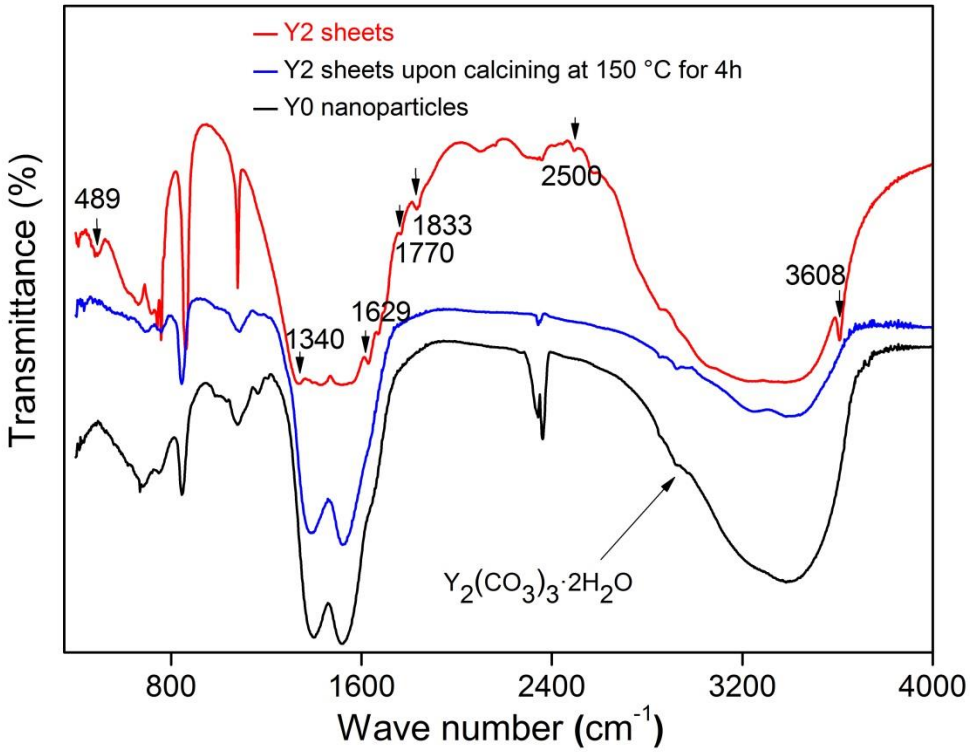

Extended Data Figure 14 | FTIR spectra of the samples. The peaks marked by the arrows verify the existence of NH_4^+ in Y2 ($(NH_4) \cdot Y(CO_3)_2 \cdot H_2O$) micron-sized sheet.

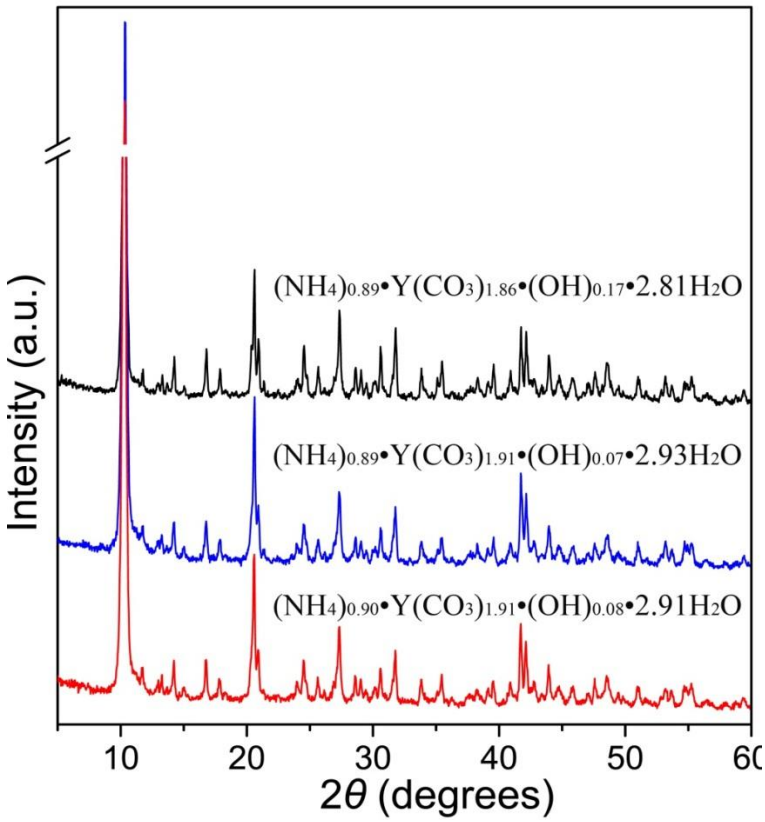

Extended Data Figure 15 | Powder XRD patterns of Y2 micron-sized sheets with slight differences in chemical compositions synthesized under different molar ratio of total NH_4HCO_3 to $Y(NO_3)_3$ (see Extended Data Table 1). No obvious differences in the patterns are observed, which indicate that there is no apparent change in its crystal structure.

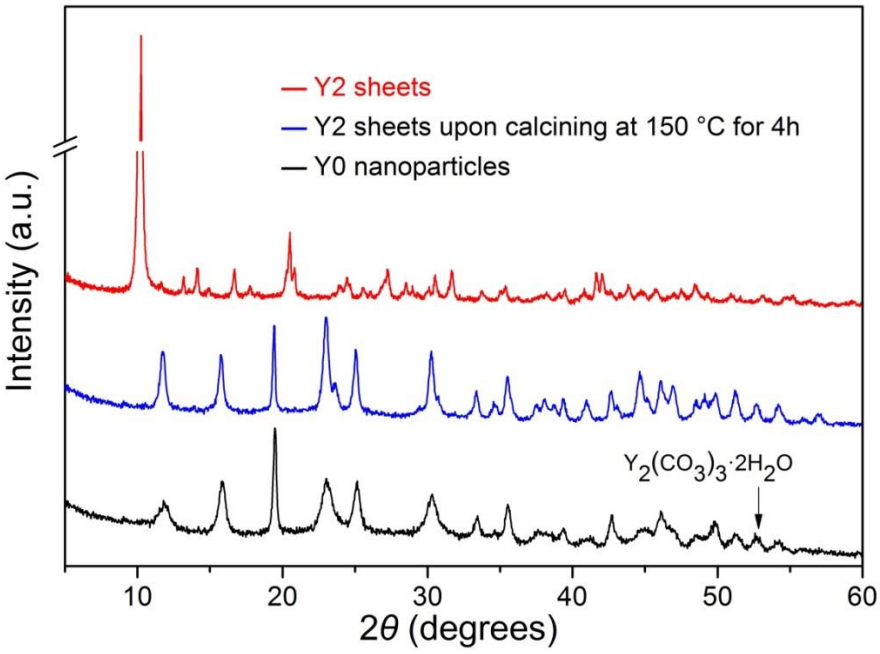

Extended Data Figure 16 | Powder XRD patterns of the samples. The patterns show the decomposition of $(NH_4)\cdot Y(CO_3)_2\cdot H_2O$ to $Y_2(CO_3)_3\cdot 2H_2O$ upon calcination at 150 ℃.

Extended Data Table 1

Table 1. Composition analysis of Y2 micron-sized sheets synthesized with the increasing addition of NH_4HCO_3.

$NH_4HCO_3/Y_2(CO_3)_3 \cdot 2H_2O$ (molar ratio)	N (wt. %)	C (wt. %)	H (wt. %)	Y (wt. %)	Composition
5/1	4.65	8.38	3.47	33.89	$(NH_4)_{0.89}Y(CO_3)_{1.86}(OH)_{0.17} \cdot 2.81H_2O$
15/1	4.52	8.33	3.41	32.45	$(NH_4)_{0.89}Y(CO_3)_{1.91}(OH)_{0.07} \cdot 2.93H_2O$
20/1	4.61	8.39	3.48	32.47	$(NH_4)_{0.90}Y(CO_3)_{1.91}(OH)_{0.08} \cdot 2.91H_2O$

Extended Discussions

S1. FTIR analysis of Y2 micron-sized sheets

By comparing the FTIR spectra of $Y_2(CO_3)_3 \cdot 2H_2O$ nanoparticles and Y2 micron-sized sheets (Extended Data Fig. 14), one can see that besides the common absorption peaks Y2 possesses particular broad peaks at 2100-2150 cm^{-1}, clear peaks at 489 cm^{-1} and 3608 cm^{-1}, and a few slight peaks as marked in Extended Data Fig. 14, indicating the presence of NH_3 and H_2O (refs[34-36]). Especially, the peak at 1340 cm^{-1} is characteristic of a hydrated yttrium ammine carbonate (Dolphin 1977, cited in ref[37]). The above peaks disappear (Extended Data Fig. 14) after the calcination of Y2 at 150 ℃ for 4h, indicating the escape of ammonia coming from decomposition of Y2 and verifying the existence of NH_4^+ in Y2.

S2. Chemical composition analysis of Y2 micron-sized sheets

The element analyses show that the chemical composition of Y2 is $(NH_4)_x \cdot Y(CO_3)_y (OH)_z \cdot nH_2O$ ($0 < x < 1$, $1.5 < y < 2$, $0 < z < 1$, $x + 3 = 2y + z$, as listed in Table S1), which is hardly affected by the molar ratio of total NH_4HCO_3 to $Y(NO_3)_3$ when the ratio is greater than 5/1. Previous researches have indicated that the precise chemical composition of well crystallized Y2 is $(NH_4) \cdot Y(CO_3)_2 \cdot H_2O$, and the composition change of Y2 is due to the hydrolysis of $(NH_4) \cdot Y(CO_3)_2 \cdot H_2O$ in the wash cycles, as follows[38, 39].

$$(NH_4) \cdot Y(CO_3)_2 \cdot H_2O + H_2O \rightarrow (NH_4)_x \cdot Y(CO_3)_y \cdot (OH)_z \cdot nH_2O + (NH_4)^+ + HCO_3^-, \quad (4)$$

In spite of the slight differences in chemical composition (Table S1) of Y2 arising from its hydrolysis, all of the XRD patterns of the products are identical within experimental errors (Extended Data Fig. 15), indicating that there is no apparent changes in the crystal structure, in line with the results reported in the hydrous yttrium carbonate mineral[17].

S3. XRD analysis of Y2 micron-sized sheets

There are no crystallographic data of $(NH_4) \cdot Y(CO_3)_2 \cdot H_2O$ in the JCPDS database or reported in previous studies. On the other hand, due to the small size and the preferred orientation of Y2 sheets it is difficult to determine its crystal structure experimentally. Nevertheless, since all of the yttrium carbonate double salts including adamsite-(Y) (ideally $NaY(CO_3)_2 \cdot 6H_2O$), shomiokite-(Y) (ideally $Na_3Y(CO_3)_3 \cdot 3H_2O$), lecoqite-(Y) (ideally $Na_3Y(CO_3)_3 \cdot 6H_2O$), and a newfound rare earth double carbonates $(NH_4) Gd(CO_3)_2 \cdot H_2O$ are all layered structure consisting of both YO_9/GdO_9 polyhedra layers and $Na(CO_3) \cdot H_2O/NH_4 (CO_3) \cdot H_2O$ layers[18, 40-42]. Hence, the inference that Y2 (ideally $(NH_4) \cdot Y(CO_3)_2 \cdot H_2O$) possesses layered structure with the ammonium remaining in the interlamellar space is reasonable. In fact, Y2 can be considered to be $(NH_4) Gd(CO_3)_2 \cdot H_2O$ in which gadolinium is replaced by yttrium, and shows similar properties to $(NH_4) Gd(CO_3)_2 \cdot H_2O$. For instance, $(NH_4) Gd(CO_3)_2 \cdot H_2O$ is stable until 175 ℃ (ref[42]); likewise, after calcination at 150 ℃ Y2 is decomposed to $Y_2(CO_3)_3 \cdot 2H_2O$ (Extended Data Fig. 16).

Hence, it can be concluded that Y2 is isostructural to $(NH_4) Gd(CO_3)_2 \cdot H_2O$, and possesses layered structure composed of YO_9 polyhedra layers and $NH_4 (CO_3) \cdot H_2O$ layers.

32. Philippini, V., Vercouter, T., Chaussé, A. & Vitorge, P. Precipitation of ALn(CO3)2•H2O and Dy2(CO3)3•xH2O compounds from aqueous solutions for A+ = Li+, Na+, K+, Cs+, NH4+ and Ln3+ = La3+, Nd3+, Eu3+, Dy3+. . *J. Solid State Chem.* **181**, 2143-2154, doi:http://dx.doi.org/10.1016/j.jssc.2008.04.030 (2008).
33. https://en.wikipedia.org/wiki/Rate-determining_step, and references therein.
34. Waldron, R. D. & Hornig, D. F. Infrared Spectra and Structure of Crystalline Ammonia Hydrates. *J. Am. Chem. Soc.* **75**, 6079-6080, doi:10.1021/ja01119a540 (1953).
35. Bertie, J. E. & Morrison, M. M. The infrared spectra of the hydrates of ammonia, NH3·H2O and 2NH3·H2O at 95K *The Journal of Chemical Physics* **73**, 4832-4837 (1980).
36. Baum, O., Giesen, T. F. & Schlemmer, S. High-resolution infrared measurements on HSOH: Analysis of the OH fundamental vibrational mode. *J. Mol. Spectrosc.* **247**, 25-29, doi:10.1016/j.jms.2007.10.005 (2008).
37. Aiken, B., Hsu, W. P. & Matijevic, E. Preparation and Properties of Monodispersed Colloidal Particles of Lanthanide Compounds: III, Yttrium(III) and Mixed Yttrium(III)/Cerium(III) Systems. *J. Am. Ceram. Soc.* **71**, 845-853 (1988).
38. Li, Y. X. *et al.* The composition and crystalline phase type of products obtained by precipitating yttrium ion with ammonium bicarbonate. *Chinese Journal of Inorganic Chemistry* **18**, 1138-1142 (2002).
39. Li, Y. X., Hu, P. G., He, X. B., Gu, Z. Y. & Li, M. Formation Process of Crystalline Ammonium Yttrium Carbonate Double Salt. *Journal of the Chinese Society of Rare Earths* **18**, 79-81 (2000).
40. Grice, J. D. The crystal structure of shomiokite-(Y). *The Canadian Mineralogist* **34**, 649-655 (1996).
41. Pekov, I. V. *et al.* LECOQITE-(Y), Na3Y(CO3)3 6H2O, A NEW MINERAL SPECIES FROM MONT SAINT-HILAIRE, QUEBEC, CANADA. *The Canadian Mineralogist* **48**, 95-104, doi:10.3749/canmin.48.1.95 (2010).
42. Rogow, D. L., Swanson, C. H., Oliver, A. G. & Oliver, S. R. J. Two related gadolinium aquo carbonate 2-D and 3-D structures and their thermal, spectroscopic, and paramagnetic properties. *Inorg. Chem.* **48**, 1533-1541 (2009).